polymers

MDPI

Article

Anionic Effect on Electrical Transport Properties of Solid $Co^{2+/3+}$ Redox Mediators

Ravindra Kumar Gupta *, Ahamad Imran and Aslam Khan

King Abdullah Institute for Nanotechnology, King Saud University, Riyadh 11451, Saudi Arabia; aimran@ksu.edu.sa (A.I.); aslamkhan@ksu.edu.sa (A.K.)

* Correspondence: rgupta@ksu.edu.sa

Abstract: In a solid-state dye-sensitized solar cell, a fast-ion conducting ($\sigma_{25^\circ C} > 10^{-4}$ S cm^{-1}) solid redox mediator (SRM; electrolyte) helps in fast dye regeneration and back-electron transfer inhibition. In this work, we synthesized solid $Co^{2+/3+}$ redox mediators using a [$(1-x)$succinonitrile: x poly(ethylene oxide)] matrix, LiX, Co(tris-2,2′-bipyridine)$_3$(bis(trifluoromethyl) sulfonylimide)$_2$, and Co(tris-2,2′-bipyridine)$_3$(bis(trifluoromethyl) sulfonylimide)$_3$ via the solution-cast method, and the results were compared with those of their acetonitrile-based liquid counterparts. The notation x is a weight fraction (=0, 0.5, and 1), and X represents an anion. The anion was either bis(trifluoromethyl) sulfonylimide [$TFSI^-$; ionic size, 0.79 nm] or trifluoromethanesulfonate [$Triflate^-$; ionic size, 0.44 nm]. The delocalized electrons and a low value of lattice energy for the anions made the lithium salts highly dissociable in the matrix. The electrolytes exhibited $\sigma_{25^\circ C} \approx 2.1 \times 10^{-3}$ (1.5×10^{-3}), 7.2×10^{-4} (3.1×10^{-4}), and 9.7×10^{-7} (6.3×10^{-7}) S cm^{-1} for x = 0, 0.5, and 1, respectively, with X = $TFSI^-$ ($Triflate^-$) ions. The log σ–T^{-1} plot portrayed a linear curve for x = 0 and 1, and a downward curve for x = 0.5. The electrical transport study showed $\sigma(TFSI^-) > \sigma(Triflate^-)$, with lower activation energy for $TFSI^-$ ions. The anionic effect increased from x = 0 to 1. This effect was explained using conventional techniques, such as Fourier transform infrared spectroscopy (FT-IR), X-ray diffractometry (XRD), X-ray photoelectron spectroscopy (XPS), scanning electron microscopy (SEM), UV–visible spectroscopy (UV-vis), differential scanning calorimetry (DSC), and thermogravimetric analysis (TGA).

Keywords: dye-sensitized solar cells; solid electrolytes; PEO; electrical conductivity; anionic effect

Citation: Gupta, R.K.; Imran, A.; Khan, A. Anionic Effect on Electrical Transport Properties of Solid $Co^{2+/3+}$ Redox Mediators. *Polymers* **2024**, *16*, 1436. https://doi.org/10.3390/polym16101436

Academic Editors: Thang Phan Nguyen and Vu Khac Hoang Bui

Received: 17 October 2023
Revised: 4 April 2024
Accepted: 16 May 2024
Published: 19 May 2024

1. Introduction

Solar cells convert sunlight energy into electrical energy without producing harmful greenhouse gases, which is one of the crucial factors in climate change [1,2]. Amongst various types of solar cells, only solid-state dye-sensitized solar cells (DSSCs) are beneficial in high-temperature regions such as Gulf countries [3]. The conversion efficiency decreases in the high-temperature region and when there is a low angle of sunlight incidence on the solar cells, except for DSSCs [1,2]. The exception occurs due to redox mediators (electrolytes). The solid nature of a redox mediator makes DSSCs scalable in manufacturing and eliminates the odds of a liquid or gel counterpart. The electrolyte participates in the following redox reactions: oxidation at the working electrode for dye regeneration, and reduction of the oxidized ions at the counter electrode. The reaction speed at the electrolyte/electrode interface largely controls DSSC efficiency. The speed depends on the electrical conductivity (σ) of the redox mediator. Therefore, a solid redox mediator (SRM) with $\sigma_{25^\circ C}$ greater than 10^{-4} S cm^{-1} is highly desirable for the fast movement of the redox couple. For a review, see references [4,5].

Solvent-free solid electrolytes with a redox couple of I^-/I_3^- have been known about since 2002 [6,7]. These electrolytes generally have the form of a matrix (-plasticizer)-MI-I_2, where M represents a cation [6–19]. The matrix is generally a solid polymer, e.g., poly(ethylene oxide), abbreviated as PEO [6,7,10], or a plastic crystal, e.g., succinonitrile

(SN) [20,21]. Table S1 in the Supplementary Information lists all used abbreviations. Plasticizers, such as low-molecular-weight polymers [22–25], synthetic resins [26,27], ionic liquids [28–30], quantum dots [31], inorganic insulators [6,7], biopolymers [13], plastic crystals [32–37], and nanoclays [38], have been applied with PEO to decrease its crystallinity. Cations are either inorganic [28–30] or organic [20,39]. It was also observed that the σ-value increases with increasing size of the cation, revealing its plasticizing property [39,40].

Recently, Gupta et al. [3] synthesized the first solid $Co^{2+/3+}$ redox mediator. They utilized [(1 − *x*)SN: *x*PEO] as a matrix with *x* = 0, 0.5, and 1 in a weight fraction. Li-bis(trifluoromethyl) sulfonylimide was used as a source of Li^+ ions. As a Co^{2+}/Co^{3+} source, a mix of Co(tris-2,2′-bipyridine)$_3$(bis(trifluoromethyl) sulfonylimide)$_2$ and Co(tris-2,2′-bipyridine)$_3$ (bis(trifluoromethyl) sulfonylimide)$_3$ was employed. The bis(trifluoromethyl) sulfonylimide ion or $(CF_3SO_2)_2N^-$ is commonly abbreviated to $TFSI^-$. The ligand, tris-(2,2′-bipyridine), shortened generally to bpy, binds the central cobalt ion. Figure S1 shows the chemical structure of ionic salts and matrices for comparison. As mentioned earlier, both SN and PEO are very good solid matrices, offering nitrile and ether, respectively, for ion transport in addition to the dissolution and complexation of ionic salt [32–35]. Specifically, SN is highly attractive because it acts as a solid solvent or plasticizer due to its low melting temperature (T_m~58 °C), high dielectric constant (55 at 25 °C and 62.6 at 58 °C), high molar enthalpy (139.7 kJ mol^{-1}), and high donor number (14 kcal mol^{-1} at 25 °C) [41]. LiTFSI provides Li^+ ions, boosting dye regeneration and, thereby, the photocurrent. The $TFSI^-$ ion has delocalized electrons with a low value of lattice energy, which increases the dissociability of ionic salt in a solvent or polymer [42]. This anion also has a large ionic size of 0.79 nm [43] and low ionic mobility [42], making it less contributory to the total electrical conductivity. The cobalt salts Co(bpy)$_3$(TFSI)$_2$ and Co(bpy)$_3$(TFSI)$_3$ provide Co^{2+} and Co^{3+} redox species, respectively [44]. Owing to the large size of Co^{2+} (0.13 nm) and Co^{3+} (0.11 nm) ions [41], accompanied by the excellent plasticizing properties of $TFSI^-$ ions and succinonitrile, SRMs achieved $\sigma_{25^\circ C}$ of 2.1 × 10^{-3} S cm^{-1} for *x* = 0, 7.2 × 10^{-4} S cm^{-1} for *x* = 0.5, and 9.7 × 10^{-7} S cm^{-1} for *x* = 1, compared with $\sigma_{25^\circ C}$ of 1.7 × 10^{-2} S cm^{-1} for acetonitrile (ACN)-based liquid redox mediators (LRMs).

$LiCF_3SO_3$ is one of the lithium salts that is highly used for preparing solid polymer electrolytes for lithium-ion batteries [45]. The anion $CF_3SO_3^-$ is generally written as $Triflate^-$ for trifluoromethanesulfonic acid. Similar to the $TFSI^-$ ion, this anion coordinates weakly with a cation and therefore does not allow ion pairing [46]. This anion has an ionic size of 0.44 nm, which is smaller to that of the $TFSI^-$ ion. LiTriflate possesses higher values of donor number and ionic mobility, and lower values of molecular weight and dissociation constant, than LiTFSI. LiTriflate, therefore, possesses a lower value of $\sigma_{25^\circ C}$ in a mixture of solvents [42]. In this study, we replaced the LiTFSI of [(1 − *x*)SN: *x*PEO]-LiTFSI-Co salts with LiTriflate to show the anionic effect on the electrical transport properties of SRMs. As previously mentioned, *x* = 0, 0.5, and 1 in the weight fraction. Hereafter, lithium salt is represented by LiX, where X = $TFSI^-$ or $Triflate^-$. The molar composition and preparatory methods for the SRM [(1 − *x*)SN: *x*PEO]-LiX-Co salts are identical. We also prepared ACN-based liquid counterparts (LRMs) identically, as reported by Mathew et al. [44], for comparison. The preparation of the SRMs with *x* = 0 was identical to that of the LRMs. We used the conventional method (solution-cast) of preparation for the PEO-based SRMs (*x* = 0.5 and 1). The anionic effect on the electrical transport properties was explained using Fourier transform infrared spectroscopy (FT-IR), X-ray diffractometry (XRD), X-ray photoelectron spectroscopy (XPS), scanning electron microscopy (SEM), UV–visible spectroscopy (UV-vis), differential scanning calorimetry (DSC), and thermogravimetric analysis (TGA).

2. Materials and Methods

The highly pure chemicals (*cf.* Table S2) were purchased and used without purification. The ACN-based LRMs and SN-based SRMs were synthesized using 0.1 M LiX, 0.25 M Co(bpy)$_3$(TFSI)$_2$, and 0.06 M Co(bpy)$_3$(TFSI)$_3$ in ACN and SN, respectively, under stirring

at 65 °C for 24 h [3,44]. The PEO-based SRMs with x = 0.5 and 1 were synthesized using the solution-cast method [32–35]. The SRMs with x = 1 underwent a complete replacement of SN with PEO, followed by rigorous stirring in acetonitrile at 65 °C for 48 h, casting on a Teflon Petri dish, and drying under a nitrogen gas atmosphere at room temperature. The SRMs with x = 0.5 were synthesized similarly. The redox mediators were characterized using conventional techniques, such as impedance spectroscopy (IS), FT-IR, XRD, XPS, SEM, UV-vis, DSC, and TGA, which are described in the Supplementary Information (*cf.* Table S3) [3,47]. Table S4 lists the equipment used for the measurements.

3. Results and Discussion

Impedance spectroscopy is a tool used to study the electrical transport properties of an electrolyte [48,49]. A complex impedance plot, widely known as the Nyquist plot, helps to deduce bulk resistance (R_b) and, thereby, the electrical conductivity of the electrolyte. Figure 1 shows Nyquist curves of the SRM [$(1 - x)$SN: xPEO]-LiX-Co salts along with their liquid counterparts (LRMs) at 25 °C. Here, x = 0, 0.5, and 1, and X = $TFSI^-$ and $Triflate^-$. In this figure, region (I) indicates a linear trend in the low-frequency domain because of the blocking-electrode effect, and region (II) corresponds to a semi-circle in the high-frequency domain because of the ionic diffusion effect [48,49]. The Nyquist curve can be fitted using an equivalent circuit [49], $R_{s,I} + (R_b \| C_1)_I + C_{2,II}$, where the notations have their usual meaning. For example, R_s stands for series resistance due to leads, R_b for bulk resistance, C_1 for chemical capacitance, and C_2 for double-layer capacitance. The LRMs exhibited nearly identical and perfect trends: a linear curve in region (I) and a semi-circle in region (II). Having a plastic crystal phase, the SRMs with x = 0 had a semi-circle similar to those of SN-LiI-I_2 [21], but with a less prominent blocking-electrode effect. In addition, the semi-circle was slightly suppressed relative to those of the LRM-based redox mediators. The SRMs with x = 1 showed largely suppressed semi-circles, most probably because of the semi-crystalline nature of the PEO [50]. The SRMs with x = 0.5 portrayed region (I) only. We found a similar pattern for the (SN-PEO)-MI-I_2 (M = Li^+ or K^+) SRMs [34,35]. This indicated the formation of amorphous domains by the short and entangled polymer chains induced by the plasticizing properties of succinonitrile [51,52]. Figure 1 also portrays the anionic effect. Relative to $Triflate^-$, $TFSI^-$ resulted in a low value of bulk resistance, as marked by an arrow. This was associated with a smaller semi-circle and a prominent linear trend, except for the redox mediator with x = 0.

We evaluated the $\sigma_{25°C}$ values of liquid and solid redox mediators using the values of the R_b, thickness, and area of the electrolyte. Table 1 lists the average values of $\sigma_{25°C}$. The LRMs achieved $\sigma_{25°C} \approx 1.7 \times 10^{-2}$ S cm^{-1} for X = $TFSI^-$ and $\approx 1.6 \times 10^{-2}$ S cm^{-1} for X = $Triflate^-$, as reported earlier for liquid electrolytes [42]. We recently attained $\sigma_{25°C}$ $\approx 10^{-3}$ S cm^{-1} for SN-LiI-I_2, because of the solid solvent nature of SN [21]. We achieved similar $\sigma_{25°C}$ values, $\approx 2.1 \times 10^{-3}$ S cm^{-1} for X = $TFSI^-$ and $\approx 1.5 \times 10^{-3}$ S cm^{-1} for X = $Triflate^-$ for the SRMs with x = 0. Compared with the LRMs, these values are less than an order of magnitude. The complete replacement of SN by PEO decreased the $\sigma_{25°C}$ value to $\approx 9.7 \times 10^{-7}$ S cm^{-1} for X = $TFSI^-$ and $\approx 6.3 \times 10^{-7}$ S cm^{-1} for X = $Triflate^-$, which are considerably less than three orders of magnitude. A poor $\sigma_{25°C}$ value was observed previously for several PEO-based solid I^-/I_3^- redox mediators and occurred due to high PEO crystallinity, hindering ion transport [34,35]. The redox mediators with x = 0.5 achieved a $\sigma_{25°C}$ value of $\approx 7.2 \times 10^{-4}$ S cm^{-1} for X = $TFSI^-$ and $\approx 3.1 \times 10^{-4}$ S cm^{-1} for X = $Triflate^-$. These values are more than two orders of magnitude higher than those of the redox mediators with x = 1 and nearly an order of magnitude lower than those of the redox mediators with x = 0. We found similar values (3–7 $\times 10^{-4}$ S cm^{-1}) for the (PEO-SN) Blend-MI-I_2 (M = Li^+ and K^+) SRMs, too [34,35]. This is due to the plasticizing nature of SN, which offers more amorphous regions for ion transport. One can note that $TFSI^-$ resulted in a better $\sigma_{25°C}$ value than $Triflate^-$, specifically for the PEO-based redox mediators. This is due to several factors, such as the large ionic size; lower values of lattice energy, donor

numbers, and ionic mobility; and higher values of the molecular weight and dissociation constant of $TFSI^-$ [42].

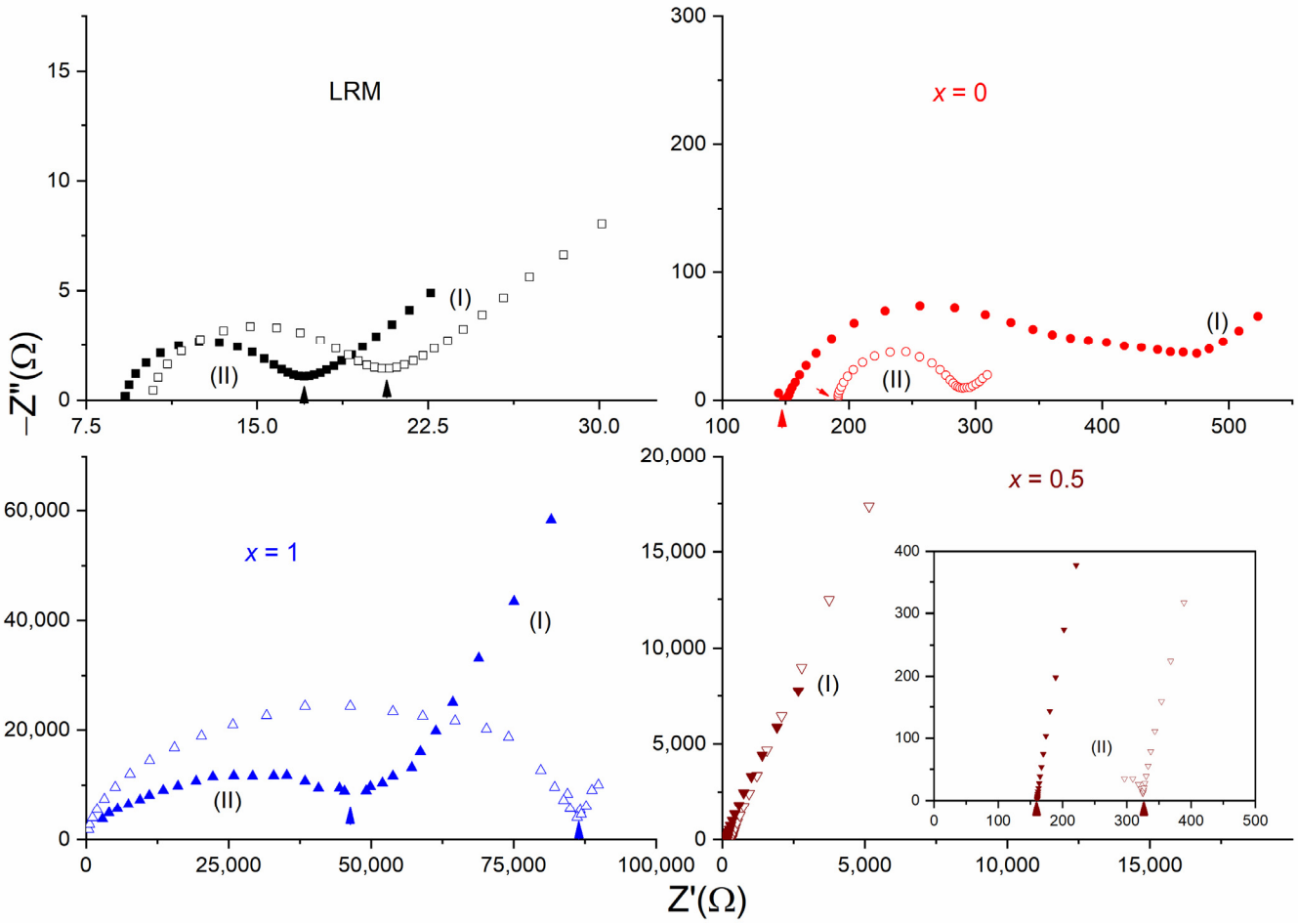

Figure 1. Nyquist curves of SRM [(1 − *x*)SN: *x*PEO]-LiX-Co salts (*x* = 0, 0.5, and 1) along with their liquid counterparts (LRMs) at 25 °C for anions, X = $TFSI^-$ (solid symbols), and $Triflate^-$ (open symbols). (I) and (II) correspond to low- and high-frequency regions, respectively.

Table 1. Electrical transport properties of SRM [(1 − x)SN: *x*PEO]-LiX-Co salts (*x* = 0, 0.5, and 1; X = $TFSI^-$ or $Triflate^-$). LRM, ACN-based liquid counterpart.

x (Wt. Fraction)	$\sigma_{25°C}$ (S cm^{-1})		Log $\sigma - T^{-1}$ Nature	Activation Energy (eV) in Regions I and II	
	$TFSI^-$	$Triflate^-$		$TFSI^-$	$Triflate^-$
0	2.1×10^{-3}	1.5×10^{-3}	Arrhenius	0.56 (I), 0.16 (II)	0.77 (I), 0.13 (II)
0.5	7.2×10^{-4}	3.1×10^{-4}	VTF	0.05	0.06
1	9.7×10^{-7}	6.3×10^{-7}	Arrhenius	1.07 (I), 0.36 (II)	1.22 (I), 0.44 (II)
LRM	1.7×10^{-2}	1.6×10^{-2}	Arrhenius	0.15	0.16

Figure 2 shows the log $\sigma - T^{-1}$ curves of the SRM [(1 − x)SN: *x*PEO]-LiX-Co salts (*x* = 0, 0.5, and 1; X = $TFSI^-$ or $Triflate^-$) and their liquid counterparts (LRMs). The SRMs with *x* = 0 and 1 showed a linear trend similar to the LRMs, SN-LiI-I_2, and PEO-KI-I_2, revealing Arrhenius-type behavior of ion transport in the form of $\sigma = \sigma_o \exp[-E_a/k_BT]$ with the help of molecules or polymeric chains, where σ_o, E_a, and k_B are the pre-exponential factor, activation energy, and Boltzmann constant, respectively [21,32,35]. The SRMs with *x* = 0.5, on the other hand, had downward curves, just like the Blend-MI-I_2. This showed Vogel–Tamman–Fulcher (VTF)-type behavior because of the formation of the amorphous phase. The VTF-type trend is expressed as $\sigma = \sigma_o T^{-½} \exp[-B/k_B(T - T_o)]$, where *B* and

T_o are the pseudo-activation energy and free-volume temperature, respectively. The inset of Figure 2 exhibits a linear $\log(\sigma T^{½}) - (T - T_o)^{-1}$ curve for SRMs with $x = 0.5$. We summarized the nature of redox mediators in Table 1. We also evaluated the values of E_a and B from the slopes of the linear curves of redox mediators and listed them in Table 1 for comparison. In this table, regions I and II correspond to the temperatures before and after the melting temperature of SRMs with $x = 0$ and 1. Both the SRMs, $x = 0$ and 1, possessed E_a-values of more than 0.3 eV in the solid-state region (region-I), making them useless for device applications [53]. In contrast, the SRMs with $x = 0.5$ possessed quite a low B-value ≈ 0.06 eV, which was similar to those of Blend-MI-I_2 [34,35]. Table 1 also shows lower activation energy values for the $TFSI^-$-based redox mediators. As mentioned earlier, this is due to the several beneficial properties of $TFSI^-$.

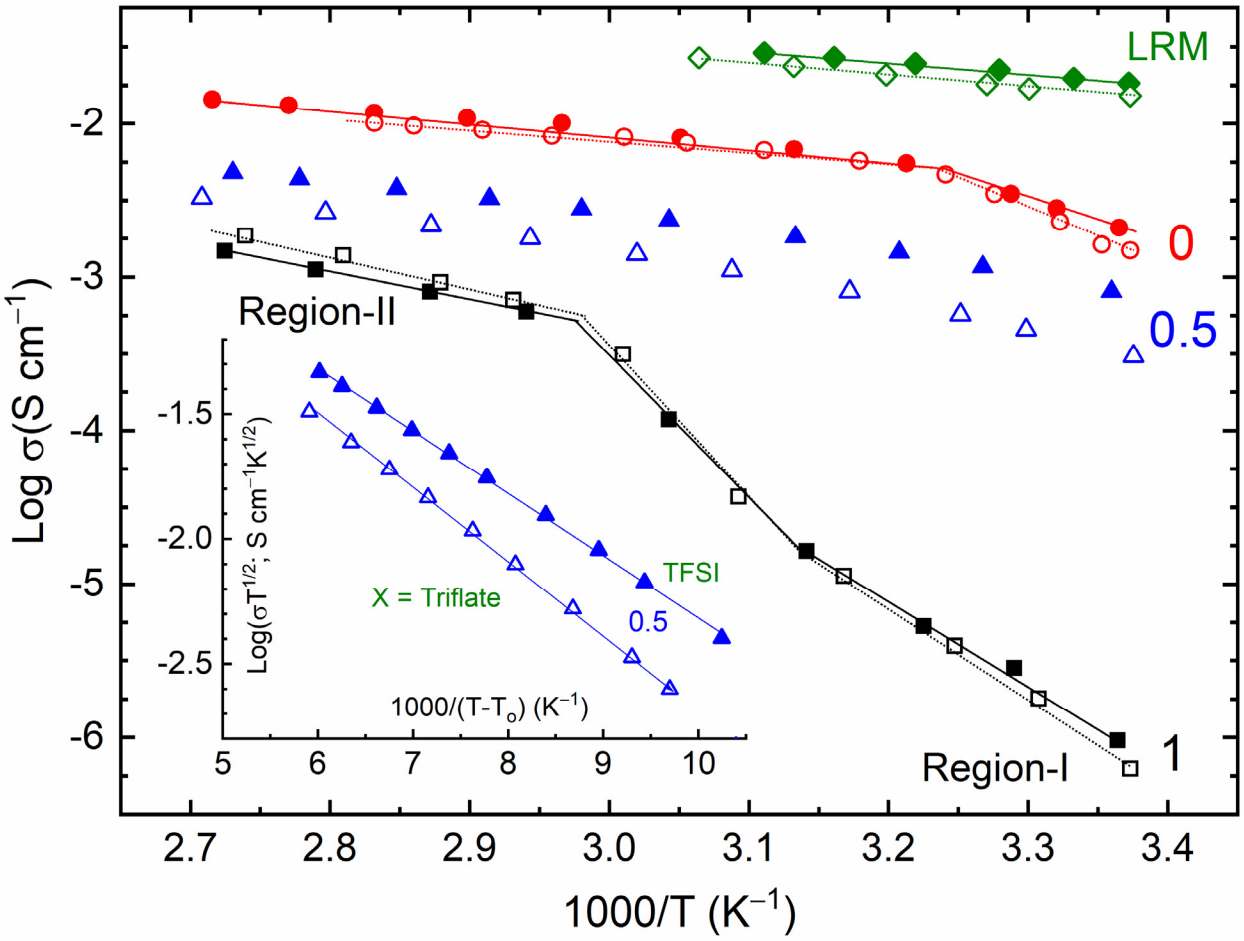

Figure 2. Log σ vs. T^{-1} curves of SRM [$(1 - x)$SN: xPEO]-LiX-Co salts with $x = 0$, 0.5, and 1. Inset: Vogel–Tamman–Fulcher (VTF) plots for SRMs with $x = 0.5$. X = $TFSI^-$ ions (filled symbols) and $Triflate^-$ ions (open symbols). LRMs, ACN-based liquid counterparts. For regions I and II, please see the text.

FT-IR spectroscopy is a tool for understanding matrix–salt interactions [3,34,35]. Interestingly, all the ingredients of the solid and liquid redox mediators are IR-active. Figure 3 shows the FT-IR spectra of SRM [$(1 - x)$SN: xPEO]-LiX-Co salts with $x = 0$, 0.5, and 1 and their liquid counterparts (LRMs) for X = $TFSI^-$ and $Triflate^-$. This also shows vibrational peaks of the matrices, solvent, and ionic salts [3,54]. The vibrational peaks of $TFSI^-$ with their assignments are as follows: 513 and 571 cm^{-1} ($\delta_{a,SO2}$), 602 cm^{-1} ($\delta_{a,SO2}$), 654 cm^{-1} ($\delta_{a,SO2}$), 739 cm^{-1} ($\nu_{s,SNS}$), 789 cm^{-1} ($\nu_{a,SNS}$), 1059 cm^{-1} ($\nu_{a,SNS}$; free), 1136 cm^{-1} ($\nu_{s,SO2}$; free), 1197 cm^{-1} ($\nu_{a,CF3}$; free), 1228 cm^{-1} ($\nu_{s,CF3}$; paired), 1333 cm^{-1} ($\nu_{a,SO2}$; paired), and 1353 cm^{-1} ($\nu_{a,SO2}$; free) [55,56]. $Triflate^-$ showed its presence through the peaks 521 cm^{-1}

($\delta_{a,SO3}$), 576 cm^{-1} ($\delta_{a,SO3}$), 641 cm^{-1} ($\delta_{a,SO3}$), 766 cm^{-1} ($\delta_{s,CF3}$), 1032 cm^{-1} ($\nu_{s,SO3}$; free), 1156 cm^{-1} ($\nu_{a,CF3}$; free), 1165 cm^{-1} ($\nu_{a,CF3}$; paired), 1226 cm^{-1} ($\nu_{s,CF3}$; free), 1258 cm^{-1} ($\nu_{a,SO3}$; paired), 1272 cm^{-1} ($\nu_{a,SO3}$; free), and 1300 cm^{-1} (paired) [57–59]. The cobalt salts have peaks of $TFSI^-$ as well as a bpy ring structure (616, 767, 1229, 1453, and 1470 cm^{-1} [60]). Here, we used the notations ν for stretching, δ for bending, s for symmetric, and a for asymmetric mode. It is worth mentioning that the peak position of free ions remains unaltered with a change in the concentration of ionic salt [55,56]. We also noticed that several modes of $TFSI^-$ merge with those of cobalt salts. Those of $Triflate^-$ exhibited overlapping in several modes with those of $TFSI^-$, too.

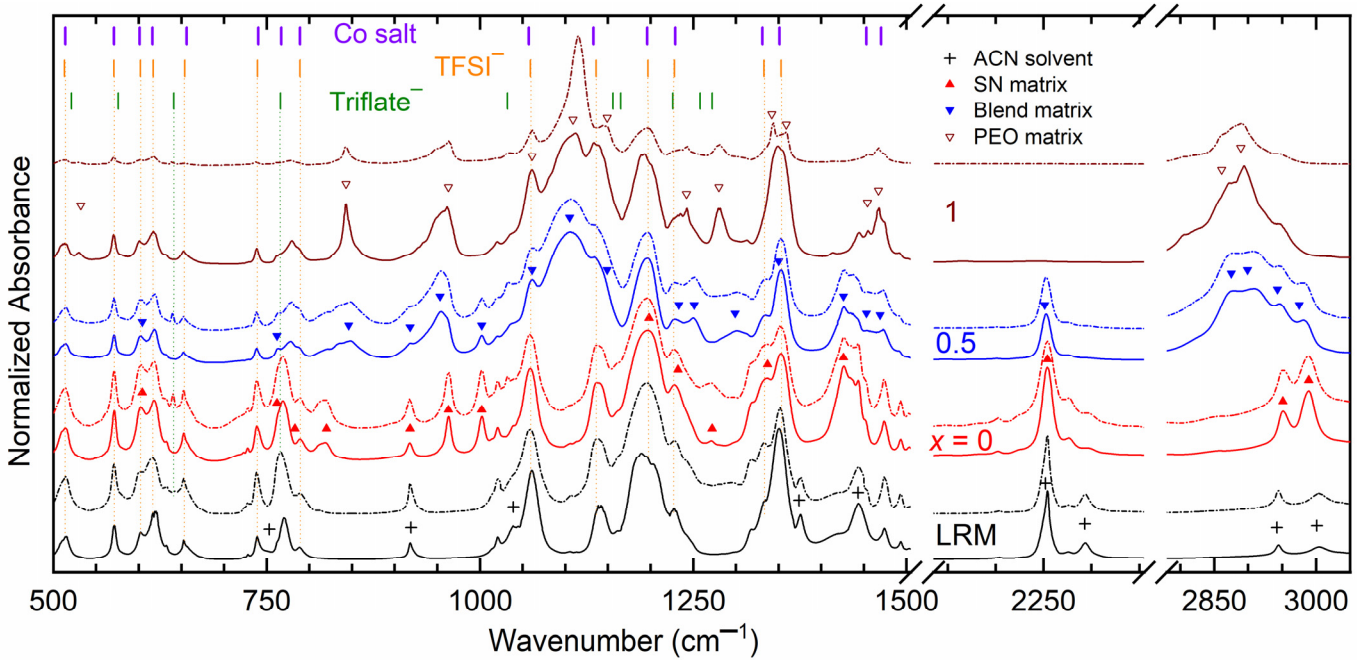

Figure 3. FT-IR spectra of SRM [(1 − *x*)SN: *x*PEO]-LiX-Co salts (*x* = 0, 0.5, and 1). LRM, ACN-based liquid counterpart. X = $TFSI^-$ (solid lines) or $Triflate^-$ (dotted lines). This also includes vibrational peaks of matrices, solvent, and ionic salts (vertical lines).

FT-IR spectroscopy showed the least interaction between the solvent and salt for the LRMs. This was indicated by the least change in the positions of the modes for the solvent and salts, except at 739 cm^{-1} (753 cm^{-1} for ACN solvent) for both anions. Also, the ion pairing peak at 1228 cm^{-1} is present as a shoulder, revealing a large number of free ions for transport with the weakest ion pairing, which resulted in $\sigma_{25°C} > 10^{-2}$ S cm^{-1} for both anions. The SRMs with $x = 0$ exhibited a minimal level of interaction between the SN matrix and salt. The mediators showed a minimal change in the positions of the modes for SN and salts. The change was noticed mainly at 769 cm^{-1} (762 cm^{-1}; SN; δ_{CH2}), 1228 cm^{-1} (1233 cm^{-1}; SN; t_{CH2}), 1443 cm^{-1} (1453 cm^{-1}; ring), and 1474 cm^{-1} (1470 cm^{-1}; ring) for both anions. The notations δ and t are the bending and twisting modes, respectively. The peak at 1228 cm^{-1} as a shoulder depicts the presence of ion pairs, too. The mediators therefore possessed lower $\sigma_{25°C}$ values ≈ 10^{-3} S cm^{-1} for both anions. The SRMs with $x = 0.5$ showed a slightly higher level of interaction between the blend matrix and salt. The interaction was noticed through changes at 778 cm^{-1} (762 cm^{-1}; Blend; δ_{CH2}), 1472 cm^{-1} (1469 cm^{-1}; Blend; δ_{CH2}), 2253 cm^{-1} (2251 cm^{-1}; Blend; $\nu_{s,C\equiv N}$), 2907 ($TFSI^-$) or 2905 ($Triflate^-$) cm^{-1} (2899 cm^{-1}; Blend; $\nu_{a,CH2}$), and 2981 ($TFSI^-$) or 2980 ($Triflate^-$) cm^{-1} (2975 cm^{-1}; Blend; $\nu_{a,CH2}$). In addition, the mediators depicted peaks at 1227 and 1334 cm^{-1}, revealing ion pairing. Being uncharged and the same size as anions, coordinated ions have higher mobility in the polymeric matrix, resulting in more amorphous regions for ion transport [55,61]. This also reduces the number of free

ions and the polymer matrix–salt interaction [55,61]. The anionic effect was observed in the $\nu_{a,CH2}$ mode only. The larger size of $TFSI^-$ led to a higher blue shift in the $\nu_{a,CH2}$ mode, indicating a higher C−H bond contraction for forming more amorphous regions and, thereby, improving the $\sigma_{25^\circ C}$ value [32,34,35,62]. The SRMs with $x = 1$ portrayed the highest level of interaction between the PEO matrix and salt. This was due to the changes at 780 ($TFSI^-$) or 777 ($Triflate^-$) cm^{-1} (767 cm^{-1}; ring), 1112 ($TFSI^-$) or 1115 ($Triflate^-$) cm^{-1} (1109 cm^{-1}; PEO; $\nu_{s,COC}$), 1134 ($TFSI^-$) or 1144sh ($Triflate^-$) cm^{-1} (1149 cm^{-1}; PEO; ν_{CC}), 1349 ($TFSI^-$) or 1343 ($Triflate^-$) cm^{-1} (1342 cm^{-1}; PEO; $\omega_{s,CH2}$), 2872 ($TFSI^-$) or 2860 ($Triflate^-$) cm^{-1} (2861 cm^{-1}; PEO; $\nu_{s,CH2}$), and 2894 ($TFSI^-$) or 2890 ($Triflate^-$) cm^{-1} (2889 cm^{-1}; PEO; $\nu_{s,CH2}$). These clearly show the anionic effect, where $TFSI^-$ ions are more effective for C−H bond contraction and amorphous region formation, and therefore higher electrical conductivity. It is also noticeable that the ion pairing peaks neither were prominent nor appeared as shoulders; in fact, they overlapped with those of the PEO.

The level of interaction between the matrix and salt in the redox mediators is observed in the following order: LRM < $x = 0 < 0.5 < 1$. This order is the same for the anionic effect, too. We quantified the matrix–salt interaction by evaluating the relative intensity, $\Delta I = I_{1105}/I_{1196}$, for both anions of redox mediators, where I_{1105} stands for intensity at 1105 cm^{-1} for the $\nu_{s,COC}$ mode of PEO, and I_{1196} for the strongest peak at 1196 cm^{-1} for the $\nu_{a,CF3}$ mode of ionic salts. Figure 4 shows the relative intensity of LRMs and SRMs for both anions. The LRMs and SRMs ($x = 0$) possessed $\Delta I = 0$ for both anions, indicating the least interaction between the solvent or matrix and ionic salt. The value of ΔI(X = $TFSI^-$) was ≈ 1.2 for the SRMs with $x = 0.5$ and 1, while the PEO-based SRMs with $x = 0.5$ and 1 had a higher value of ΔI(X = $Triflate^-$): 1.34 and 3.4, respectively. This revealed an increase in the level of interaction from $x = 0.5$ to 1, resulting in a hindrance in ion transport and a decrease in $\sigma_{25^\circ C}$ value. This also demonstrated that ΔI(X = $Triflate^-$) is greater than ΔI(X = $TFSI^-$), indicating the anionic effect. The XRD study, discussed below, also supports this result.

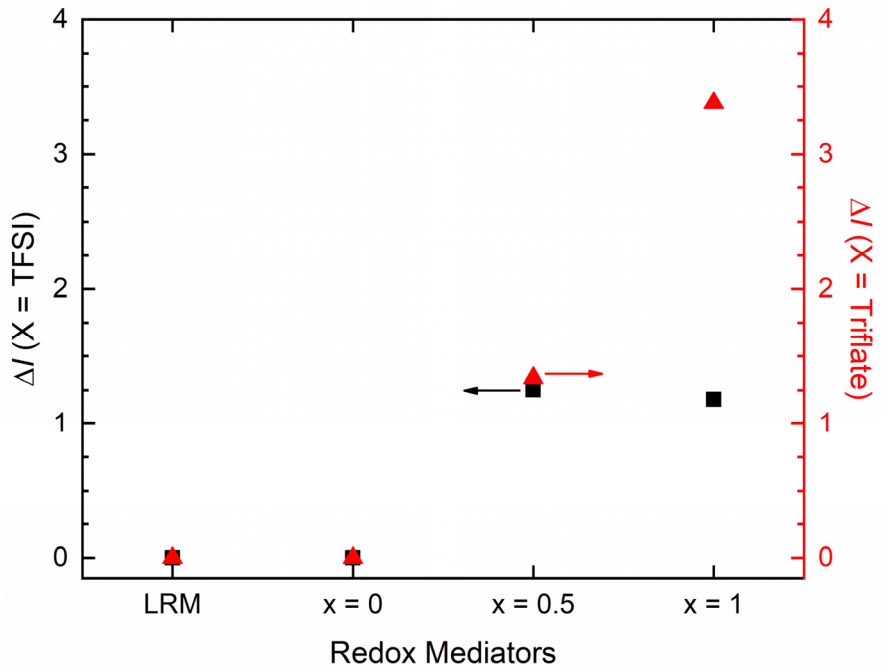

Figure 4. Relative intensity, ΔI, of SRM [$(1 - x)$SN: xPEO]-LiX-Co salts with $x = 0$, 0.5, and 1, and X = $TFSI^-$ and $Triflate^-$, along with those of their liquid counterparts (LRMs).

Figure 5 shows the XRD patterns of the SRM [$(1 - x)$SN: xPEO]-LiX-Co salts with $x = 0$, 0.5, and 1 for X = $TFSI^-$ (solid line) and $Triflate^-$ (dotted line). Table 2 lists the observed peaks of redox mediators with $x = 0$ and 1, which are small and broad as well

as slightly shifted relative to the matrix (SN: 2θ ≈ 19.7° and 28.1°; PEO: 2θ ≈ 19.2° and 23.3° [32]). The patterns of these mediators had no peaks for other ingredients. In contrast, the redox mediators with x = 0.5 exhibited no peaks. An amorphous peak appeared at 27.6° for X = $TFSI^-$ and 23.1° for X = $Triflate^-$. These indicate disorder in the SN molecules, eutectic phase formation, and amorphous phase formation in the PEO or blend matrix [3,21,33–35,63]. For the blend-based redox mediators (x = 0.5), PEO acted as an impurity, abolishing the crystalline structure of the SN in the presence of ions [3,33–35]. The absence of reflection peaks of the ionic salts also confirmed complete dissolution and complexation of the salts. The anionic effect is visible for all the redox mediators, x = 0 − 1. The redox mediator with x = 0 exhibited relatively stronger reflection peaks of succinonitrile for X = $TFSI^-$ than $Triflate^-$. The latter is indicative of eutectic phase formation, as indicated by the DSC study, which is discussed later [21,63]. The redox mediator (x = 1) had stronger reflection peaks of PEO for X = $Triflate^-$ than $TFSI^-$, revealing a higher level of PEO crystallinity and, thereby, a lower value of electrical conductivity. The SEM results, discussed later, corroborate these results.

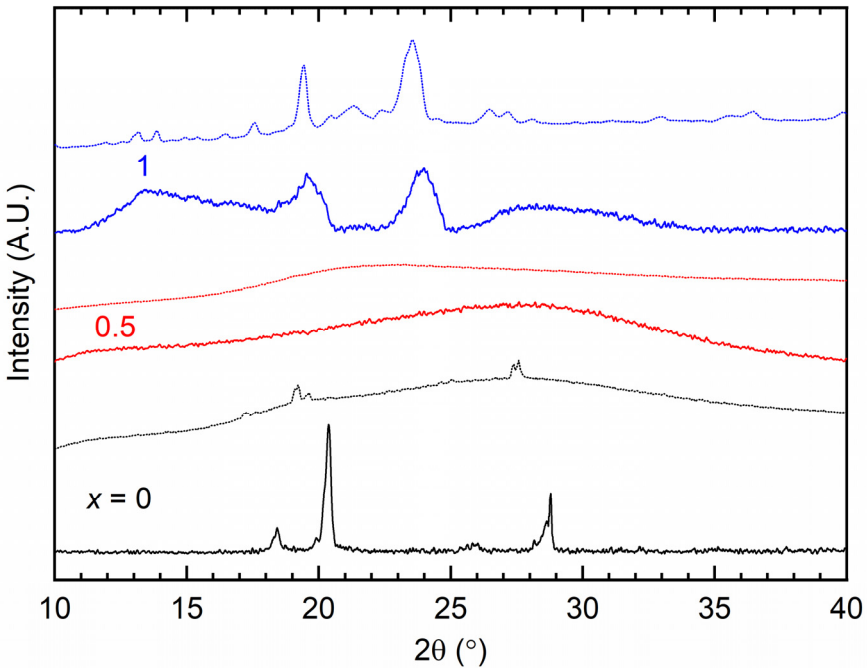

Figure 5. XRD patterns of SRM [(1 − x)SN: xPEO]-LiX-Co salts, where x = 0, 0.5, and 1. X = $TFSI^-$ (solid line) and $Triflate^-$ (dotted line).

Table 2. Angle (2θ) and transmittance (T) of SRM [(1 − x)SN: xPEO]-LiX-Co salts, where x = 0, 0.5, and 1. X = $TFSI^-$ and $Triflate^-$. I, II, and III stand for UV-A, visible, and near-IR regions, respectively.

x (Wt. Fraction)	2θ (°)		T (%) in Regions I, II, and III	
	$TFSI^-$	$Triflate^-$	$TFSI^-$	$Triflate^-$
0	20.4, 28.8	19.2, 27.6	0 (I), 21.6 (II), 48.7 (III)	0 (I), 15.1 (II), 46.8 (III)
0.5	27.6	23.1	88.1 (I), 99.8 (II), 110.5 (III)	68.8 (I), 91.8 (II), 105.4 (III)
1	19.5, 24	19.4, 23.6	49.6 (I), 78.9 (II), 99.9 (III)	45.4 (I), 71.9 (II), 93.3 (III)

X-ray photoelectron spectroscopy is a tool used to study the interaction between ingredients at the surface [47,64–68]. Figure S2 shows the survey spectra of SRM [(1 − x)SN: xPEO]-LiX-Co salts (x = 0, 0.5, and 1; X = $TFSI^-$ and $Triflate^-$). The survey spectrum was corrected to fix the C 1 s peak at 284.6 eV [64–66]. The survey spectra depicted S 2p, C 1 s, N 1 s, O 1 s, and F 1 s elements for all redox mediators. However, only the redox

mediators with x = 0 exhibited Ti 2p peaks. The presence of this peak can be attributed to the enhanced penetration of SN-based electrolytes into the pores of the TiO_2 layer and the creation of a remarkably thin film on TiO_2, facilitated by the solid solvent characteristic of SN. The SEM image demonstrates the infiltration and development of a thin coating of SN-based electrolyte on the TiO_2 substrate, as described in the next paragraph. The TiO_2 substrate is anticipated to exhibit a substantial accumulation of PEO-based redox mediators (x = 0.5 and 1), hence impeding the examination of the electrolyte/TiO_2 interface. The peak's position, intensity, and width (full width at half maximum) were determined through the fitting of the smoothed and baseline-corrected spectrum. Figures S3–S5 depict the best-fit plots of different elements of SRMs with x = 0, 0.5, and 1, respectively. The left and right columns are for SRMs, with X = $TFSI^-$ and $Triflate^-$, respectively. Figure 6 shows smoothed and baseline-corrected XPS spectra of the S 2p, C 1 s, N 1 s, O 1 s, and F 1 s elements for the SRM [(1 − x)SN: xPEO]-LiX-Co salts with x = (a) 0, (b) 0.5, and (c) 1, where X = $TFSI^-$ and $Triflate^-$. Figure 6a also portrays the spectra of the Ti 2p element. The peaks can be assigned in light of previously reported studies [47,64–68]. The SRMs depicted a small-height S 2p peak because of the $-SO_2{}^-$ group at ≈168.2 eV for the spin of 3/2, associated with a shoulder peak at ≈169.8 eV for the spin of ½. The area of the C 1 s core level is the most complex. This area showed a standard mid-height peak at 284.6 eV for the alkyl (−C−C−) group associated with a strong peak at ≈286 eV for the bpy ring or −C−C−O− group, a small-height peak at ≈288.6 eV for the −C≡N group, and a distinctive small-height peak at ≈292 eV for the $–CF_3$ group. The N 1 s spectrum depicted a small-height broad peak consisting of two deconvoluted peaks because of anions at ≈398 eV and the bpy ring at ≈400 eV. The Ti 2p spectrum of the TiO_2 layer exhibited two strong and distinctive peaks at ≈458.2 eV and ≈464 eV because of the spin-orbit-coupling phenomenon. The SRMs with x = 0 portrayed two O 1 s core-level strong distinctive peaks at ≈529.8 eV and ≈532 eV because of the $-SO_2{}^-$ group in the anions. The PEO-based SRMs (x = 0.5 and 1) exhibited the strongest O 1 s peak with deconvolution of ≈531 eV and ≈532 eV because of the spin-orbit-coupling phenomenon. The redox mediators also showed a strong F 1 s core-level distinctive peak at ≈688.6 eV because of the $–CF_3$ group of anions. We divided the intensity by the width to make the ratio dimensionless. Figure 7 plots the intensity/width (=R) against the peak position for all redox mediators with x = 0, 0.5, and 1. The solid symbols represent redox mediators with X = $TFSI^-$, and open symbols denote redox mediators with X = $Triflate^-$. This figure demonstrates a shift either in the ratio ($\Delta R = R_{TFSI} - R_{Triflate}$; cf. Figure S6) or peak position (ΔP = Peak $Position_{TFSI}$ − Peak $Position_{Triflate}$; cf. Figure S7) or both, revealing an anionic effect. The level of shift differed depending on the composition and element. For example, the SRMs with x = 0 showed ΔR < 0, except for O 1 s, where ΔR > 0, too; the redox mediators with x = 0.5 depicted ΔR > 0, except for O 1 s and F 1 s, where ΔR < 0; and the redox mediators with x = 1 exhibited both positive and negative ΔR. At F 1 s, the negative shift was minimum for x = 0.5 and maximum for x = 0. The SRMs with x = 0 showed ΔP > 0 for S 2p, C 1 s, O 1 s, and F 1 s core levels, and ΔP < 0 for N 1 s. The redox mediators with x = 0.5 exhibited $\Delta P \geq 0$ for S 2p, C 1 s, and F 1 s core levels, and ΔP < 0 for N 1 s and O 1 s. The redox mediators with x = 1 depicted $\Delta P \geq 0$ for all core levels.

The mesoporous TiO_2 layer was subjected to impregnation with a solid redox mediator, [(1 − x)SN: xPEO]-LiX-Co salts, with x = 0, 0.5, and 1, and X = $TFSI^-$ or $Triflate^-$. Figure 8 shows SEM images of the surface of the impregnated mesoporous TiO_2. The pores of mesoporous TiO_2 were penetrated by redox mediators with x = 0 due to the solid solvent feature of SN. On the other hand, it was observed that the redox mediators with x = 0.5 and 1 failed to effectively impregnate the pores of the mesoporous TiO_2, as evidenced by the subpar photovoltaic performance [69]. PEO-containing redox mediators (x = 0.5 and 1) exhibited fibril-like structures due to the presence of polymeric chains of PEO [10,34,35]. Succinonitrile, as a solid solvent and plasticizer, exerted significant influence over the fibril architectures [34,35]. A similar trend may be observed in the case of SRMs, where the surface smoothness exhibited a reduction from x = 0.5 to 1, as well as from X = $TFSI^-$

to Triflate$^-$. These findings suggest a rise in the crystallinity of PEO within the range of x = 0.5 to 1, as well as from X = TFSI$^-$ to Triflate$^-$. This observation is supported by the transmittance spectra of the redox mediators (x = 0, 0.5, and 1; X = TFSI$^-$ to Triflate$^-$), which are described below.

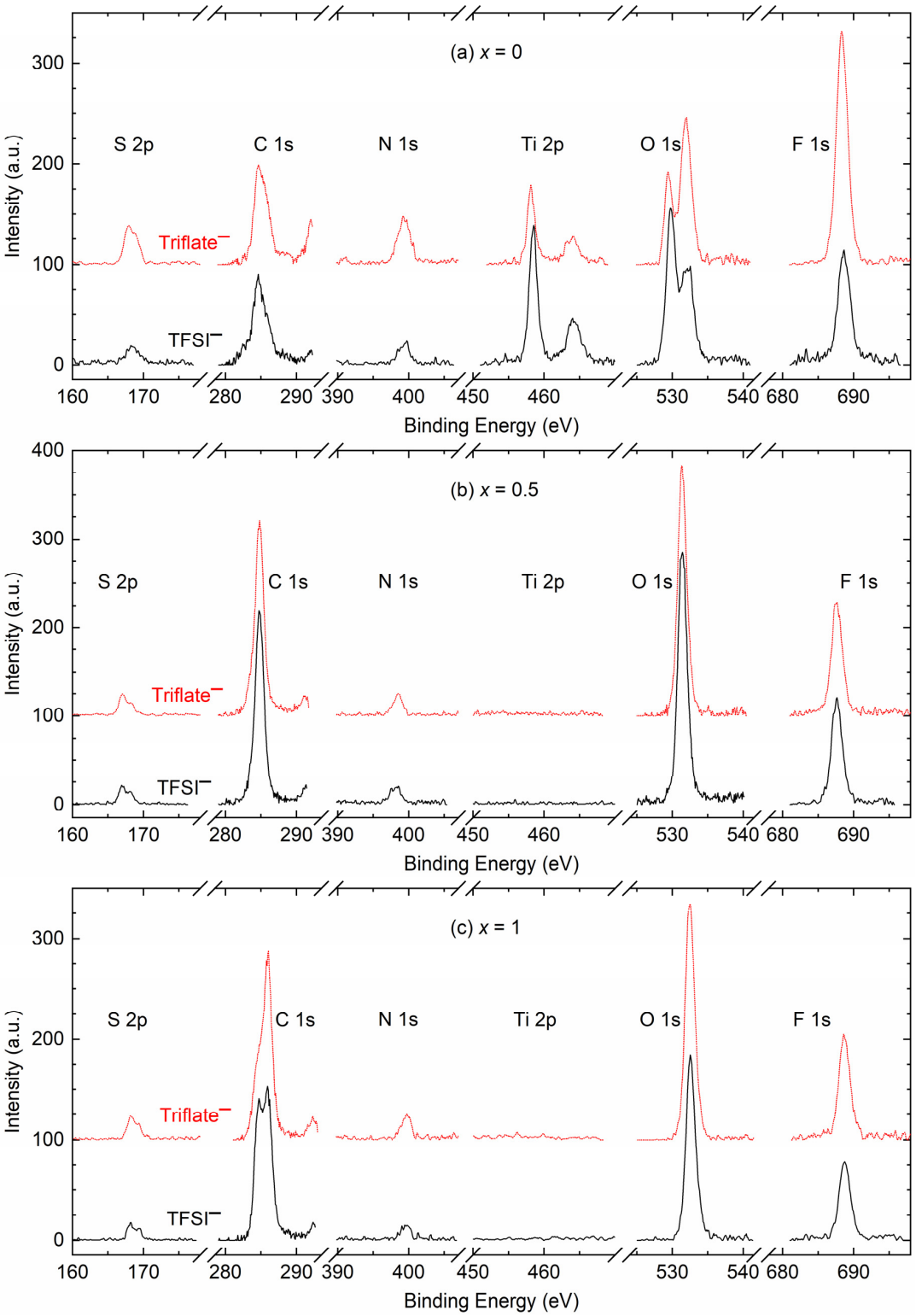

Figure 6. XPS spectra of different elements of SRM [(1 − x)SN: xPEO]-LiX-Co salts, where x = (**a**) 0, (**b**) 0.5, and (**c**) 1. X = TFSI$^-$ (solid line) and Triflate$^-$ (dotted line).

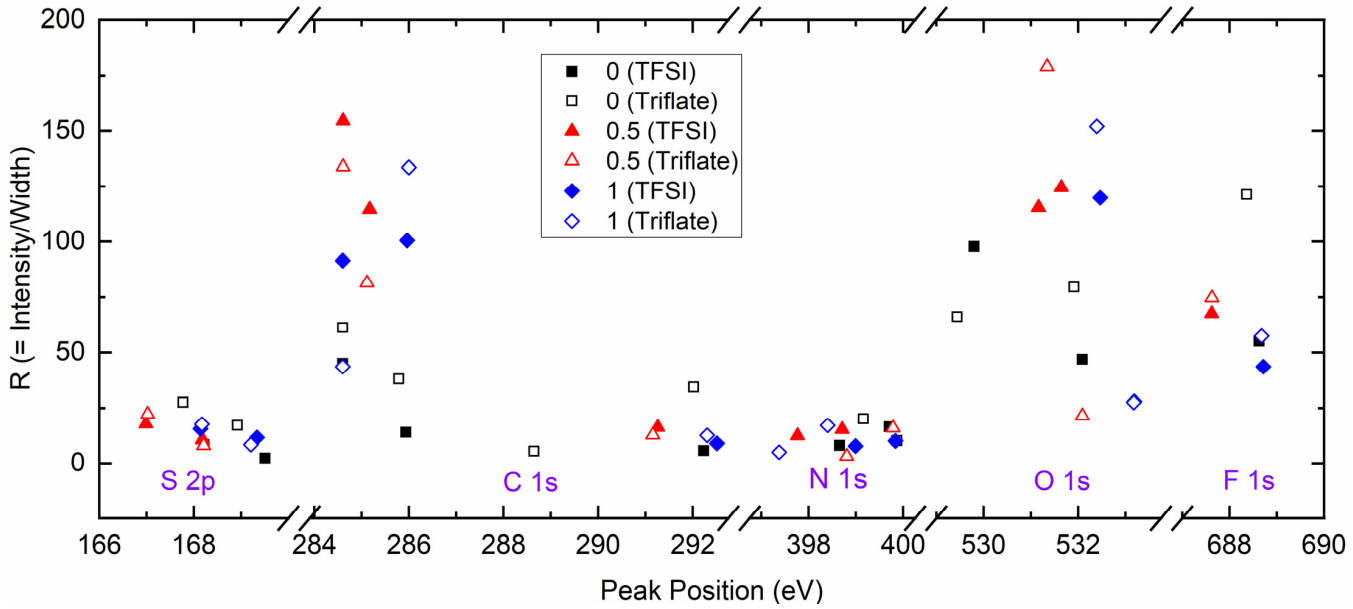

Figure 7. Plot of ratio (R) of intensity with width vs. peak position for different elements of SRM [(1 − *x*)SN: *x*PEO]-LiX-Co salts, where *x* = 0, 0.5, and 1. X = $TFSI^-$ (solid symbols) and $Triflate^-$ (open symbols).

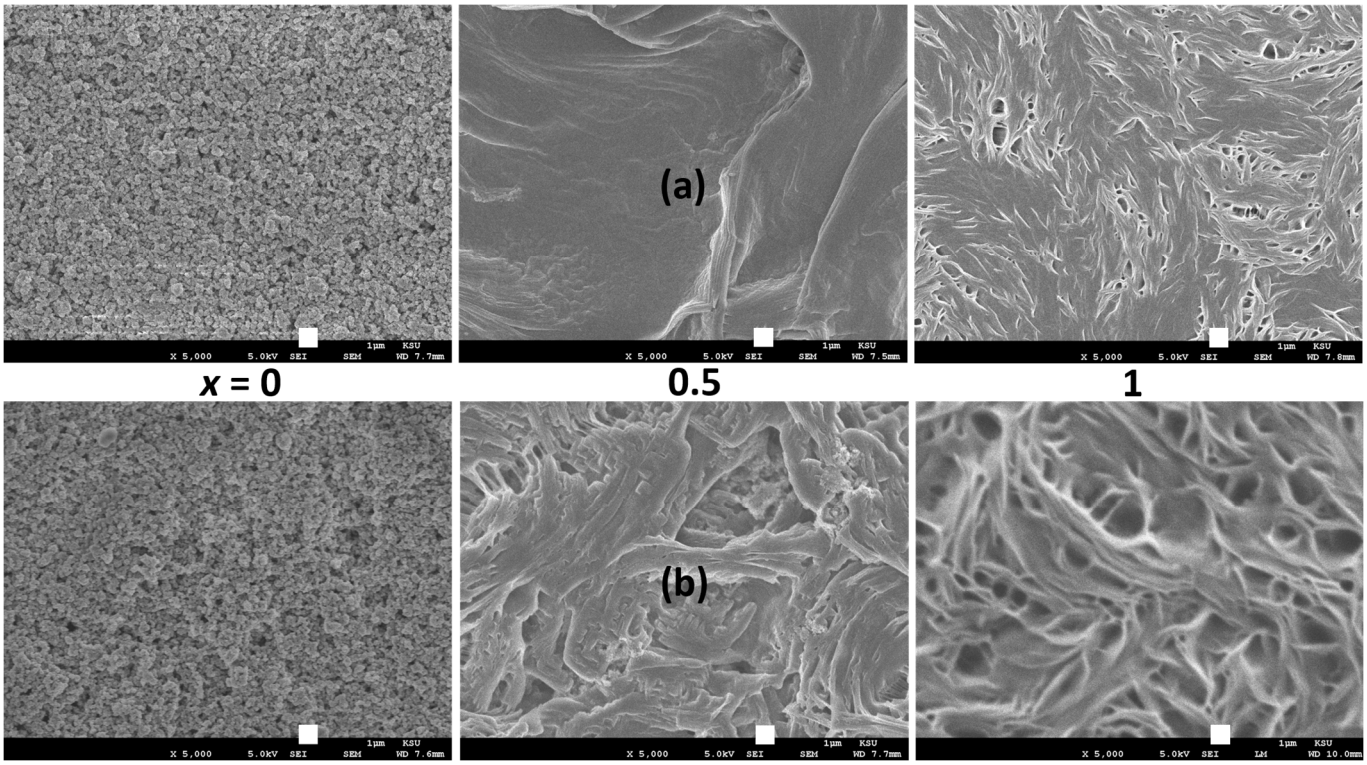

Figure 8. SEM images for the surface of SRM [(1 − *x*)SN: *x*PEO]-LiX-Co salts with *x* = 0, 0.5, and 1, infiltrated in the mesoporous TiO_2. X = (**a**) $TFSI^-$ and (**b**) $Triflate^-$. Scale bar, 1 µm.

Figure 9 shows the transmittance spectra of SRM [(1 − *x*)SN: *x*PEO]-LiX-Co salts (*x* = 0, 0.5, and 1) for X = $TFSI^-$ and $Triflate^-$. We can divide the spectra into three regions: I (UV-A; 350 nm), II (visible; 555 nm), and III (near-IR; 900 nm). Table 2 summarizes the transmittance of the SRMs, which can be compared with those of their liquid counterparts (LRMs): 13.9% (I), 99.9% (II), and 99.7% (III) for X = $TFSI^-$, and 3.3% (I), 99.9% (II), and

101.9% (III) for X = Triflate$^-$. The SRMs with x = 0 and 1 had poor transmittance values; however, blending SN and PEO largely improved the transmittance. This is due to a decrease in PEO crystallinity because of the plasticizing properties of the SN [35]. Table 2 portrays the anionic effect, too, where TFSI$^-$ led to better transmittance than Triflate$^-$. This is due to a decrease in PEO crystallinity, as pointed out by the DSC results, which are discussed below.

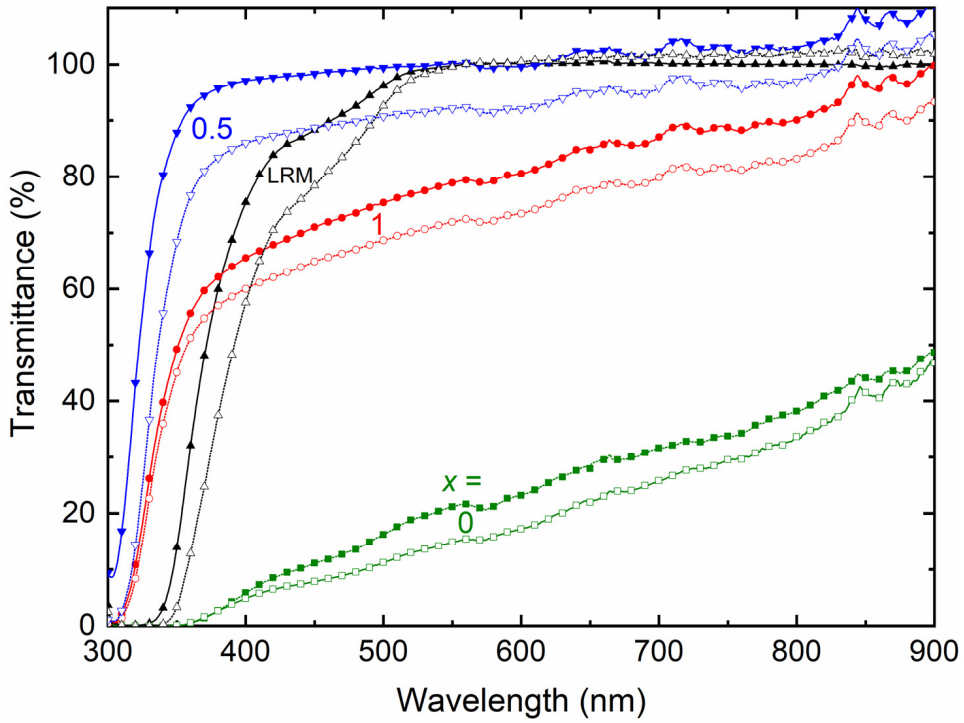

Figure 9. Transmittance spectra of SRM [(1 − x)SN: xPEO]-LiX-Co salts with x = 0, 0.5, and 1. LRM, ACN-based liquid counterpart. X = TFSI$^-$ (filled symbols) and Triflate$^-$ (open symbols).

Figure 10 shows the DSC curves of the SRM [(1 − x)SN: xPEO]-LiX-Co salts, where x = 0, 0.5, and 1, and X = TFSI$^-$ and Triflate$^-$. The SRMs with x = 0 portrayed two endothermic peaks marked by T_{pc} and T_m for crystal-to-plastic-crystal phase transition temperature and melting temperature, respectively. Table 3 lists the values of T_{pc} and T_m for comparison. For the SN matrix, T_{pc} = –38.4 °C and T_m = 57.7 °C [21,63]. It is worth mentioning that the area of T_m-peak corresponds to the heat enthalpy or crystallinity of the redox mediator [21,32]. We observed that the position and area of T_m-peak decreased for the SRMs with x = 0 relative to the pure SN matrix. This is indicative of a decrease in the crystallinity of succinonitrile [21]. The T_{pc}-peak showed a position similar to that of the pure matrix, as observed earlier for the SN-LiI-I_2 redox mediator, however, with an increase in the area, most probably because of the SN–ionic salt interaction [21,63]. The anionic effect is also noticeable for SRMs with x = 0. For example, TFSI$^-$ resulted in a broad T_m-peak, which is indicative of the disordered plastic crystalline nature of SN. In contrast, Triflate$^-$ yielded multiplets at higher temperatures with a larger area, indicating eutectic phase formation along with the disordered plastic crystal phase of SN. TFSI$^-$ also resulted in the area (40.9) of the T_{pc}-peak being less than that for Triflate$^-$ (139.9), which is indicative of less crystallinity and, thereby, higher electrical conductivity in the TFSI$^-$-based redox mediator. The SRMs with x = 1 had a T_m-peak with values of only 63.8 °C for X = TFSI$^-$ and 65.2 °C for X = Triflate$^-$, which are less than the T_m-value of the PEO matrix (65.7 °C [32]). The area of the T_m-peak was also less than that of the PEO matrix, revealing a decrease in PEO crystallinity. These DSC curves also exhibited the anionic effect via a decrease in the position and area of the T_m-peak for X = TFSI$^-$, revealing a decrease in PEO crystallinity and, thereby, an increase in electrical conductivity [32–35].

The SRMs with x = 0.5 possessed negligibly small and broad T_m-peaks with values of only 4 °C for X = $TFSI^-$ and 7.8–26 °C for X = $Triflate^-$. These values, as well as the peak area, are less than those of the PEO-SN blend matrix ($T_m \approx 30.1$ °C [32]), indicating a decrease in PEO crystallinity. The anionic effect was visualized at the T_m-peak position and area. $TFSI^-$ led to lower values of T_m and a smaller area compared to $Triflate^-$, resulting in lower PEO crystallinity and, thereby, a higher $\sigma_{25°C}$ value. These results are also consistent with the findings of the TGA investigation, which are discussed below.

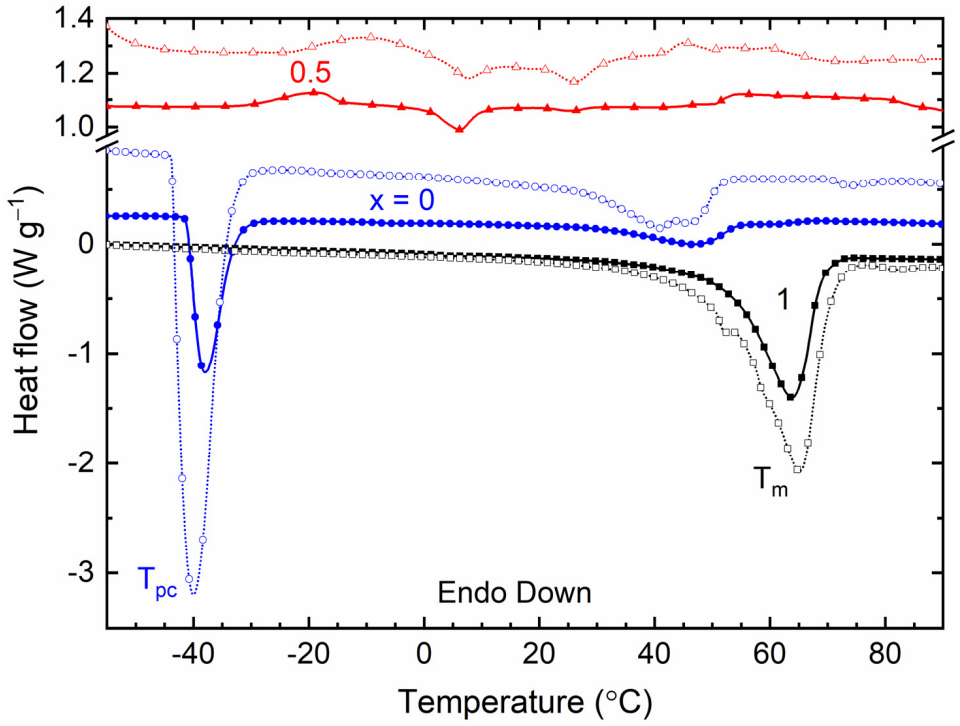

Figure 10. DSC curves of SRM [(1 − x)SN: xPEO]-LiX- Co salts with x = 0, 0.5, and 1. X = $TFSI^-$ (filled symbols) and $Triflate^-$ (open symbols).

Table 3. T_m, T_m-area, and T_{pc} of SRM [(1 − x)SN: xPEO]-LiX-Co salts with x = 0, 0.5, and 1. X = $TFSI^-$ and $Triflate^-$.

x (Wt. Fraction)	T_m (°C)		T_m-Area (a.u.)		T_{pc} (°C)	
	$TFSI^-$	$Triflate^-$	$TFSI^-$	$Triflate^-$	$TFSI^-$	$Triflate^-$
0	47	41 and 45.8	15.6	43.2	−37.8	−40
0.5	4	7.8 and 26	2.4	17.5	-	-
1	63.8	65.2	92.7	160.4	-	-

Figure 11 shows the TGA curves of the SRM [(1 − x)SN: xPEO]-LiX-Co salts with x = 0, 0.5, and 1 for X = $TFSI^-$ and $Triflate^-$. The initial plateau region of the curve corresponds to the thermal stability of the SRM, which is ≈75 °C for x = 0, 125 °C for x = 0.5, and 200 °C for x = 1. These values are similar to those of the pure matrices [32]. The SRMs with x = 0 and 1 exhibited one-step dropping due to the decomposition of the matrix, while the mediators with x = 0.5 showed two-step dropping due to the decomposition of the SN and PEO matrices [3,32]. These curves also portrayed an anionic effect via the degradation phenomenon. $TFSI^-$ resulted in more rapid degradation compared to $Triflate^-$, particularly for SRMs with x = 0.5 and 1. This is because $TFSI^-$-based redox mediators have lower PEO crystallinity.

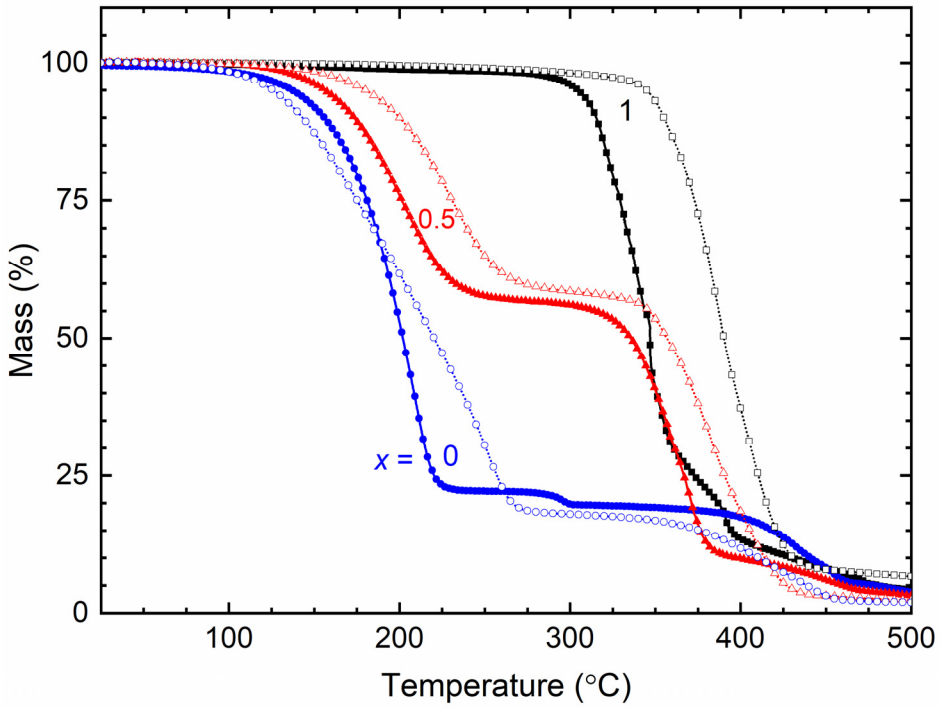

Figure 11. TGA curves of SRM [(1 − *x*)SN: *x*PEO]-LiX-Co salts with *x* = 0, 0.5, and 1. X = $TFSI^-$ ions (filled symbols) and $Triflate^-$ ions (open symbols).

As mentioned earlier, an SRM with $\sigma_{25^\circ C} > 10^{-4}$ S cm^{-1} and $E_a < 0.3$ eV is required to regenerate dye molecules faster at the TiO_2/dye/electrolyte interface and, thereby, inhibit back-electron transfer [6–19]. Faster dye regeneration via the faster oxidation of ionic species results in a higher photocurrent and cell efficiency. This also results in faster ionic species regeneration. However, the higher mass of metal ions, e.g., Co^{2+}/Co^{3+}, slows down their diffusion in DSSCs, which decreases the concentration of metal ions at the TiO_2/dye/electrolyte interface, resulting in poor cell efficiency [69,70]. Hence, it is imperative to enhance the porosity of the mesoporous TiO_2 film in order to accommodate a greater number of ionic species at the interface [70]. It is also necessary to have TiO_2 pores that are water-free because water changes the surface of TiO_2 and decreases cell efficiency [4,71]. In the present scenario, due to their superior electrical transport and optical properties, the DSSCs with $TFSI^-$-based SRMs are expected to perform better than those with $Triflate^-$-based SRMs. However, porosity at the TiO_2/dye/electrolyte interface needs to be optimized by utilizing a mixture of large and small anatase TiO_2 nanoparticles [69,70,72–74]. Therefore, we will perform DSSC fabrication and characterizations in the future.

4. Conclusions

We studied the electrical transport properties of SRM [(1 − *x*)SN: *x*PEO]-LiX-Co salts (*x* = 0, 0.5, and 1; X = $TFSI^-$ and $Triflate^-$), and the results were compared with those of their acetonitrile-based liquid counterparts (LRMs). The LRMs exhibited $\sigma_{25^\circ C} \approx 10^{-2}$ S cm^{-1}. The SRMs achieved $\sigma_{25^\circ C} \approx 10^{-3}$ S cm^{-1} for *x* = 0, $>10^{-4}$ S cm^{-1} for *x* = 0.5, and $\approx 10^{-6}$ S cm^{-1} for *x* = 1. In these redox mediators, $\sigma_{25^\circ C}(TFSI^-) > \sigma_{25^\circ C}(Triflate^-)$ and $E_a(TFSI^-) < E_a(Triflate^-)$. FT-IR spectroscopy showed the interaction and, thereby, the anionic effect in the following order: LRM < 0 < 0.5 < 1. The XRD study exhibited an increase in PEO crystallinity from *x* = 0.5 to 1, which was more for $Triflate^-$ ions. The XPS study showed a shift in the intensity/width ratio and peak position of the elements because of the anionic effect. The SEM images depicted an increase in surface roughness from *x* = 0.5 to 1, which was higher for $Triflate^-$ ions. The transmittance showed the following orders: LRM = 0 (= 0%) << 1 << 0.5 in the UV-A region, 0 << 1 << LRM ≈ 0.5

in the visible region, and 0 << 1 < 0.5 < LRM in the near-IR region. Only the SRMs with x = 0.5 showed higher transmittance in the UV-A, visible, and near-IR regions. In addition, the transmittance was higher for the $TFSI^-$ ion-based redox mediators. The DSC study exhibited the lowest T_m-peak area for x = 0.5 and the highest peak area for x = 1. The SRMs had a lower peak area for $TFSI^-$ ions. The TGA study revealed the thermal stability of SRMs, ≈75 °C for x = 0, 125 °C for x = 0.5, and 200 °C for x = 1, and degradation was faster for $TFSI^-$ ion-based redox mediators. Various studies on [(1 − x)SN: xPEO]-LiX-Co salts (x = 0, 0.5, and 1) have demonstrated similar trends despite different anions (X = $TFSI^-$ and $Triflate^-$). However, the electrical transport properties of SRMs with X = $TFSI^-$ were better than those of SRMs with X = $Triflate^-$. Owing to superior its electrical transport and optical properties, the SRM with x = 0.5 and X = $TFSI^-$ can be utilized for DSSC and tandem solar cell applications.

Supplementary Materials: The following supporting information can be downloaded at: https://www.mdpi.com/article/10.3390/polym16101436/s1, Figure S1: Chemical structure of (a) ionic salts and (b) matrices; Figure S2. XPS survey spectra of solid redox mediators, [(1 − x)SN: xPEO]-LiX-Co salts (x = 0, 0.5, and 1; X = $TFSI^-$ and $Triflate^-$); Figure S3: Best fits of XPS spectra of different elements of solid redox mediators (x = 0; X = $TFSI^-$ and $Triflate^-$). This figure also includes the best fits of XPS spectra of the Ti 2p element; Figure S4: Best fits of XPS spectra of different elements of solid redox mediators (x = 0.5; X = $TFSI^-$ and $Triflate^-$); Figure S5: Best fits of XPS spectra of different elements of solid redox mediators (x = 1; X = $TFSI^-$ and $Triflate^-$); Figure S6: A plot of ΔR (= $[\text{intensity/width}]_{TFSI}$ − $[\text{intensity/width}]_{Triflate}$) with peak position for different elements of solid redox mediators, [(1 − x)SN: xPEO]-LiX-Co salts, where x = 0, 0.5, and 1. X = $TFSI^-$ and $Triflate^-$; Figure S7: A plot of ΔP (= $[\text{peak position}]_{TFSI}$ − $[\text{peak position}]_{Triflate}$) with peak position for different elements of solid redox mediators, [(1 − x)SN: xPEO]-LiX-Co salts, where x = 0, 0.5, and 1. X = $TFSI^-$ and $Triflate^-$; Table S1: Abbreviations used in the article; Table S2: Chemicals used for the preparation of liquid and solid redox mediators; Table S3: Details of characterization techniques; Table S4: Equipment used for the measurements.

Author Contributions: Conceptualization, R.K.G.; methodology, R.K.G.; formal analysis, R.K.G., A.I. and A.K.; investigation, R.K.G., A.I. and A.K.; writing—original draft preparation, R.K.G.; writing—review and editing, R.K.G., A.K. and A.I.; supervision, R.K.G.; project administration, R.K.G.; funding acquisition, R.K.G. All authors have read and agreed to the published version of the manuscript.

Funding: This work was funded by the National Plan for Science, Technology, and Innovation (MAARIFAH), King Abdulaziz City for Science and Technology, Kingdom of Saudi Arabia (Award Number 13-ENE886-02).

Institutional Review Board Statement: Not applicable.

Data Availability Statement: The data are contained within the article.

Conflicts of Interest: The authors declare no conflict of interest.

References

1. Luque, A.; Hegedus, S. *Handbook of Photovoltaic Science and Engineering*, 2nd ed.; John Wiley & Sons, Ltd.: Chichester, UK, 2011.
2. Green, M.A.; Dunlop, E.D.; Yoshita, M.; Kopidakis, N.; Bothe, K.; Siefer, G.; Hao, X. Solar cell efficiency tables (version 63). *Prog. Photovolt. Res. Appl.* **2024**, *32*, 3–13. [CrossRef]
3. Gupta, R.K.; Shaikh, H.; Imran, A.; Bedja, I.; Ajaj, A.F.; Aldwayyan, A.S. Electrical transport, structural, optical and thermal properties of [(1-x)Succinonitrile: xPEO]-LiTFSI-Co(bpy)$_3$(TFSI)$_2$-Co(bpy)$_3$(TFSI)$_3$ solid redox mediators. *Polymers* **2022**, *14*, 1870. [CrossRef] [PubMed]
4. Hagfeldt, A.; Boschloo, G.; Sun, L.C.; Kloo, L.; Pettersson, H. Dye-sensitized solar cells. *Chem. Rev.* **2010**, *110*, 6595–6663. [CrossRef] [PubMed]
5. Munoz-Garcia, A.B.; Benesperi, I.; Boschloo, G.; Concepcion, J.J.; Delcamp, J.H.; Gibson, E.A.; Meyer, G.J.; Pavone, M.; Pettersson, H.; Hagfeldt, A.; et al. Dye-sensitized solar cells strike back. *Chem. Soc. Rev.* **2021**, *50*, 12450–12550. [CrossRef]
6. Katsaros, G.; Stergiopoulos, T.; Arabatzis, I.M.; Papadokostaki, K.G.; Falaras, P. A solvent-free composite polymer/inorganic oxide electrolyte for high efficiency solid-state dye-sensitized solar cells. *J. Photochem. Photobiol. A-Chem.* **2002**, *149*, 191–198. [CrossRef]
7. Stergiopoulos, T.; Arabatzis, I.M.; Katsaros, G.; Falaras, P. Binary polyethylene oxide/titania solid-state redox electrolyte for highly efficient nanocrystalline tio$_2$ photoelectrochemical cells. *Nano Lett.* **2002**, *2*, 1259–1261. [CrossRef]

8. Nogueira, A.F.; Longo, C.; De Paoli, M.A. Polymers in dye sensitized solar cells: Overview and perspectives. *Coord. Chem. Rev.* **2004**, *248*, 1455–1468. [CrossRef]
9. Li, B.; Wang, L.D.; Kang, B.N.; Wang, P.; Qiu, Y. Review of recent progress in solid-state dye-sensitized solar cells. *Sol. Energy Mater. Sol. Cells* **2006**, *90*, 549–573. [CrossRef]
10. Singh, P.K.; Nagarale, R.K.; Pandey, S.P.; Rhee, H.W.; Bhattacharya, B. Present status of solid state photoelectrochemical solar cells and dye sensitized solar cells using PEO-based polymer electrolytes. *Adv. Nat. Sci. Nanosci. Nanotechnol.* **2011**, *2*, 023002. [CrossRef]
11. Wu, J.H.; Lan, Z.; Lin, J.M.; Huang, M.L.; Huang, Y.F.; Fan, L.Q.; Luo, G.G. Electrolytes in dye-sensitized solar cells. *Chem. Rev.* **2015**, *115*, 2136–2173. [CrossRef]
12. Su ait, M.S.; Rahman, M.Y.A.; Ahmad, A. Review on polymer electrolyte in dye-sensitized solar cells (DSSCs). *Sol. Energy* **2015**, *115*, 452–470. [CrossRef]
13. Singh, R.; Polu, A.R.; Bhattacharya, B.; Rhee, H.W.; Varlikli, C.; Singh, P.K. Perspectives for solid biopolymer electrolytes in dye sensitized solar cell and battery application. *Renew. Sustain. Energy Rev.* **2016**, *65*, 1098–1117. [CrossRef]
14. Mehmood, U.; Al-Ahmed, A.; Al-Sulaiman, F.A.; Malik, M.I.; Shehzad, F.; Khan, A.U.H. Effect of temperature on the photovoltaic performance and stability of solid-state dye-sensitized solar cells: A review. *Renew. Sustain. Energy Rev.* **2017**, *79*, 946–959. [CrossRef]
15. Venkatesan, S.; Lee, Y.L. Nanofillers in the electrolytes of dye-sensitized solar cells—A short review. *Coord. Chem. Rev.* **2017**, *353*, 58–112. [CrossRef]
16. Iftikhar, H.; Sonai, G.G.; Hashmi, S.G.; Nogueira, A.F.; Lund, P.D. Progress on electrolytes development in dye-sensitized solar cells. *Materials* **2019**, *12*, 1998. [CrossRef] [PubMed]
17. Hasan, M.M.; Islam, M.D.; Rashid, T.U. Biopolymer-based electrolytes for dye-sensitized solar cells: A critical review. *Energy Fuels* **2020**, *34*, 15634–15671. [CrossRef]
18. Wang, N.; Hu, J.J.; Gao, L.G.; Ma, T.L. Current progress in solid-state electrolytes for dye-sensitized solar cells: A mini-review. *J. Electron. Mater.* **2020**, *49*, 7085–7097. [CrossRef]
19. Abu Talip, R.A.; Yahya, W.Z.N.; Bustam, M.A. Ionic liquids roles and perspectives in electrolyte for dye-sensitized solar cells. *Sustainability* **2020**, *12*, 7598. [CrossRef]
20. Dai, Q.; MacFarlane, D.R.; Forsyth, M. High mobility I^-/I_3^- redox couple in a molecular plastic crystal: A potential new generation of electrolyte for solid-state photoelectrochemical cells. *Solid State Ion.* **2006**, *177*, 395–401. [CrossRef]
21. Gupta, R.K.; Bedja, I.; Islam, A.; Shaikh, H. Electrical, structural, and thermal properties of succinonitrile-LiI-I_2 redox-mediator. *Solid State Ion.* **2018**, *326*, 166–172. [CrossRef]
22. Kang, M.S.; Kim, J.H.; Kim, Y.J.; Won, J.; Park, N.G.; Kang, Y.S. Dye-sensitized solar cells based on composite solid polymer electrolytes. *Chem. Commun.* **2005**, *7*, 889–891. [CrossRef]
23. Kang, M.S.; Kim, J.H.; Won, J.; Kang, Y.S. Dye-sensitized solar cells based on crosslinked poly(ethylene glycol) electrolytes. *J. Photochem. Photobiol. A-Chem.* **2006**, *183*, 15–21. [CrossRef]
24. Zhou, Y.F.; Xiang, W.C.; Chen, S.; Fang, S.B.; Zhou, X.W.; Zhang, J.B.; Lin, Y. Influences of poly(ether urethane) introduction on poly(ethylene oxide) based polymer electrolyte for solvent-free dye-sensitized solar cells. *Electrochim. Acta* **2009**, *54*, 6645–6650. [CrossRef]
25. Kang, M.S.; Kim, J.H.; Won, J.; Kang, Y.S. Oligomer approaches for solid-state dye-sensitized solar cells employing polymer electrolytes. *J. Phys. Chem. C* **2007**, *111*, 5222–5228. [CrossRef]
26. Han, H.W.; Liu, W.; Zhang, J.; Zhao, X.Z. A hybrid poly(ethylene oxide)/poly(vinylidene fluoride)/TiO_2 nanoparticle solid-state redox electrolyte for dye-sensitized nanocrystalline solar cells. *Adv. Funct. Mater.* **2005**, *15*, 1940–1944. [CrossRef]
27. Yang, Y.; Zhang, J.; Zhou, C.H.; Wu, S.J.; Xu, S.; Liu, W.; Han, H.W.; Chen, B.L.; Zhao, X.Z. Effect of lithium iodide addition on poly(ethylene oxide)-poly(vinylidene fluoride) polymer-blend electrolyte for dye-sensitized nanocrystalline solar cell. *J. Phys. Chem. B* **2008**, *112*, 6594–6602. [CrossRef]
28. Singh, P.K.; Kim, K.W.; Rhee, H.W. Electrical, optical and photoelectrochemical studies on a solid PEO-polymer electrolyte doped with low viscosity ionic liquid. *Electrochem. Commun.* **2008**, *10*, 1769–1772. [CrossRef]
29. Singh, P.K.; Kim, K.W.; Park, N.G.; Rhee, H.W. Mesoporous nanocrystalline TiO_2 electrode with ionic liquid-based solid polymer electrolyte for dye-sensitized solar cell application. *Synth. Met.* **2008**, *158*, 590–593. [CrossRef]
30. Singh, P.K.; Kim, K.W.; Rhee, H.W. Ionic liquid (1-methyl 3-propyl imidazolium iodide) with polymer electrolyte for DSSC application. *Polym. Eng. Sci.* **2009**, *49*, 862–865. [CrossRef]
31. Singh, P.K.; Kim, K.W.; Rhee, H.W. Quantum dot doped solid polymer electrolyte for device application. *Electrochem. Commun.* **2009**, *11*, 1247–1250. [CrossRef]
32. Gupta, R.K.; Kim, H.M.; Rhee, H.W. Poly(ethylene oxide): Succinonitrile—A polymeric matrix for fast-ion conducting redox-couple solid electrolytes. *J. Phys. D-Appl. Phys.* **2011**, *44*, 205106. [CrossRef]
33. Gupta, R.K.; Rhee, H.W. Highly conductive redox-couple solid polymer electrolyte system: Blend-KI-I_2 for dye-sensitized solar cells. *Adv. OptoElectron.* **2011**, *2011*, 102932. [CrossRef]
34. Gupta, R.K.; Rhee, H.W. Effect of succinonitrile on electrical, structural, optical, and thermal properties of poly(ethylene oxide)-succinonitrile/LiI-I_2 redox-couple solid polymer electrolyte. *Electrochim. Acta* **2012**, *76*, 159–164. [CrossRef]

35. Gupta, R.K.; Rhee, H.W. Plasticizing effect of K^+ ions and succinonitrile on electrical conductivity of poly(ethylene oxide)-succinonitrile/KI-I_2 redox-couple solid polymer electrolyte. *J. Phys. Chem. B* **2013**, *117*, 7465–7471. [CrossRef]
36. Gupta, R.K.; Shaikh, H.; Imran, A.; Bedja, I.; Aldwayyan, A.S. Structural, thermal, and electrical properties of poly(ethylene oxide)-tetramethyl succinonitrile blend for redox mediators. *Polymers* **2022**, *14*, 3728. [CrossRef]
37. Gupta, R.K.; Shaikh, H.; Imran, A.; Bedja, I.; Aldwayyan, A.S. Tetramethyl succinonitrile as a solid plasticizer in a poly(ethylene oxide)$_8$ -LiI-I_2 solid polymer electrolyte. *Macromol. Rapid Commun.* **2022**, *43*, e2100764. [CrossRef]
38. Gupta, R.K.; Rhee, H.W.; Bedja, I.; AlHazaa, A.N.; Khan, A. Effect of laponite$^{(R)}$ nanoclay dispersion on electrical, structural, and photovoltaic properties of dispersed poly(ethylene oxide)-succinonitrile -LiI-I_2 solid polymer electrolyte. *J. Power Sources* **2021**, *490*, 229509. [CrossRef]
39. Bhattacharya, B.; Lee, J.Y.; Geng, J.; Jung, H.T.; Park, J.K. Effect of cation size on solid polymer electrolyte based dye-sensitized solar cells. *Langmuir* **2009**, *25*, 3276–3281. [CrossRef] [PubMed]
40. Gupta, R.K.; Bedja, I. Cationic effect on dye-sensitized solar cell properties using electrochemical impedance and transient absorption spectroscopy techniques. *J. Phys. D-Appl. Phys.* **2017**, *50*, 245501. [CrossRef]
41. Lide, D.R. *CRC Handbook of Chemistry and Physics*, 89th ed.; CRC Press/Taylor and Francis: Boca Raton, FL, USA, 2009; pp. 3–6.
42. Arya, A.; Sharma, A.L. A glimpse on all-solid-state Li-ion battery (ASSLIB) performance based on novel solid polymer electrolytes: A topical review. *J. Mater. Sci.* **2020**, *55*, 6242–6304. [CrossRef]
43. Largeot, C.; Portet, C.; Chmiola, J.; Taberna, P.-L.; Gogotsi, Y.; Simon, P. Relation between the ion size and pore size for an electric double-layer capacitor. *J. Am. Chem. Soc.* **2008**, *130*, 2730–2731. [CrossRef] [PubMed]
44. Mathew, S.; Yella, A.; Gao, P.; Humphry-Baker, R.; Curchod, B.F.E.; Ashari-Astani, N.; Tavernelli, I.; Rothlisberger, U.; Nazeeruddin, M.K.; Gratzel, M. Dye-sensitized solar cells with 13% efficiency achieved through the molecular engineering of porphyrin sensitizers. *Nat. Chem.* **2014**, *6*, 242–247. [CrossRef] [PubMed]
45. Aifantis, K.E.; Kumar, R.V.; Hu, P. *Rechargeable Ion Batteries: Materials, Design, and Applications of Li-Ion Cells and Beyond*; WILEY-VCH GmbH: Weinheim, Germany, 2023.
46. Gupta, R.K.; Jung, H.Y.; Whang, C.M. Transport properties of a new Li^+ ion-conducting ormolyte: (SiO_2-PEG)-$LiCF_3SO_3$. *J. Mater. Chem.* **2002**, *12*, 3779–3782. [CrossRef]
47. Alhefeiti, M.; Chandra, F.; Gupta, R.K.; Saleh, N. Dyeing non-recyclable polyethylene plastic with photoacid phycocyanobilin from spirulina algae: Ultrafast photoluminescence studies. *Polymers* **2022**, *14*, 4811. [CrossRef]
48. Monk, P. *Fundamentals of Electroanalytical Chemistry*; John Wiley & Sons: Chichester, UK, 2001.
49. Careem, M.A.; Noor, I.S.M.; Arof, A.K. Impedance spectroscopy in polymer electrolyte characterization. In *Polymer Electrolytes: Characterization Techniques and Energy Applications*; Winie, T., Arof, A.K., Thomas, S., Eds.; Wiley: Weinheim, Germany, 2020; pp. 23–64.
50. Haq, N.; Shakeel, F.; Alanazi, F.K.; Shaikh, H.; Bedja, I.; Gupta, R.K. Utilization of poly(ethylene terephthalate) waste for preparing disodium terephthalate and its application in a solid polymer electrolyte. *J. Appl. Polym. Sci.* **2019**, *136*, 47612. [CrossRef]
51. Fan, L.Z.; Hu, Y.S.; Bhattacharyya, A.J.; Maier, J. Succinonitrile as a versatile additive for polymer electrolytes. *Adv. Funct. Mater.* **2007**, *17*, 2800–2807. [CrossRef]
52. Patel, M.; Chandrappa, K.G.; Bhattacharyya, A.J. Increasing ionic conductivity and mechanical strength of a plastic electrolyte by inclusion of a polymer. *Electrochim. Acta* **2008**, *54*, 209–215. [CrossRef]
53. Agrawal, R.C.; Gupta, R.K. Superionic solids: Composite electrolyte phase—An overview. *J. Mater. Sci.* **1999**, *34*, 1131–1162. [CrossRef]
54. Gupta, R.K.; Jung, H.Y.; Wi, C.J.; Whang, C.M. *Solid State Ionics: Trends in the New Millennium*; Chowdari, B.V.R., Prabaharan, S.R.S., Yahaya, M., Talib, I.A., Eds.; World Scientific: Singapore, 2002; pp. 369–376.
55. Wen, S.J.; Richardson, T.J.; Ghantous, D.I.; Striebel, K.A.; Ross, P.N.; Cairns, E.J. Ftir characterization of PEO + $LiN(CF_3SO_2)_2$ electrolytes. *J. Electroanal. Chem.* **1996**, *408*, 113–118. [CrossRef]
56. Rey, I.; Lassègues, J.C.; Grondin, J.; Servant, L. Infrared and raman study of the peo-litfsi polymer electrolyte. *Electrochim. Acta* **1998**, *43*, 1505–1510. [CrossRef]
57. Bernson, A.; Lindgren, J. Ion aggregation and morphology for poly(ethylene oxide)-based polymer electrolytes containing rare-earth-metal salts. *Solid State Ion.* **1993**, *60*, 31–36. [CrossRef]
58. Huang, W.; Frech, R.; Wheeler, R.A. Molecular structures and normal vibrations of trifluoromethane sulfonate ($CF_3SO_3^-$) and its lithium ion pairs and aggregates. *J. Phys. Chem.* **1994**, *98*, 100–110. [CrossRef]
59. Rhodes, C.P.; Frech, R. A symmetry-based analysis of raman and infrared spectra of the compounds (poly(ethylene oxide))$_3$ $LiCF_3SO_3$ and (poly(ethylene oxide))$NaCF_3SO_3$. *Solid State Ion.* **2000**, *136–137*, 1131–1137. [CrossRef]
60. Castellucci, E.; Angeloni, L.; Neto, N.; Sbrana, G. Ir and raman spectra of a 2,2′-bipyridine single crystal: Internal modes. *Chem. Phys.* **1979**, *43*, 365–373. [CrossRef]
61. Gupta, R.K.; Rhee, H.W. Detailed investigation into the electrical conductivity and structural properties of poly(ethylene oxide)-succinonitrile -Li$(CF_3SO_2)_2N$ solid polymer electrolytes. *Bull. Korean Chem. Soc.* **2017**, *38*, 356–363. [CrossRef]
62. Colthup, N.B.; Daly, L.H.; Wiberley, S.E. *Introduction to Infrared and Raman Spectroscopy*, 3rd ed.; Academic Press: San Diego, CA, USA, 1990.
63. Alarco, P.J.; Abu-Lebdeh, Y.; Abouimrane, A.; Armand, M. The plastic-crystalline phase of succinonitrile as a universal matrix for solid-state ionic conductors. *Nat. Mater.* **2004**, *3*, 476–481. [CrossRef] [PubMed]

64. Martin-Vosshage, D.; Chowdari, B.V.R. X-ray photoelectron spectroscopy studies on poly(ethylene oxide) with sodium triflate. *J. Electrochem. Soc.* **1993**, *140*, 3531. [CrossRef]
65. Andersson, A.M.; Herstedt, M.; Bishop, A.G.; Edström, K. The influence of lithium salt on the interfacial reactions controlling the thermal stability of graphite anodes. *Electrochim. Acta* **2002**, *47*, 1885–1898. [CrossRef]
66. Morales-Ugarte, J.E.; Santini, C.C.; Bouchet, R.; Benayad, A. New interpretation of x-ray photoelectron spectroscopy of imidazolium ionic liquid electrolytes based on ionic transport analyses. *J. Phys. Chem. B* **2020**, *124*, 7625–7635. [CrossRef]
67. Zhang, Q.; Liu, K.; Ding, F.; Li, W.; Liu, X.; Zhang, J. Enhancing the high voltage interface compatibility of $LiNi_{0.5}Co_{0.2}Mn_{0.3}O_2$ in the succinonitrile-based electrolyte. *Electrochim. Acta* **2019**, *298*, 818–826. [CrossRef]
68. Andersson, E.K.W.; Sångeland, C.; Berggren, E.; Johansson, F.O.L.; Kühn, D.; Lindblad, A.; Mindemark, J.; Hahlin, M. Early-stage decomposition of solid polymer electrolytes in li-metal batteries. *J. Mater. Chem. A* **2021**, *9*, 22462–22471. [CrossRef]
69. Gupta, R.K.; Shaikh, H.; Imran, A.; Bedja, I.; Ajaj, A.F.; Aldwayyan, A.S. *Towards All-Solid-State Dye-Sensitized Solar Cells Using Co(II/III) Redox Couple-Based Solid Polymer Electrolytes*; 13-ENE886-02; King Saud University: Riyadh, Saudi Arabia, 2023; p. 1.
70. Yella, A.; Mathew, S.; Aghazada, S.; Comte, P.; Gratzel, M.; Nazeeruddin, M.K. Dye-sensitized solar cells using cobalt electrolytes: The influence of porosity and pore size to achieve high-efficiency. *J. Mater. Chem. C* **2017**, *5*, 2833–2843. [CrossRef]
71. Juodkazis, K.; Juodkazytė, J.; Jelmakas, E.; Kalinauskas, P.; Valsiūnas, I.; Miečinskas, P.; Juodkazis, S. Photoelectrolysis of water: Solar hydrogen–achievements and perspectives. *Opt. Express* **2010**, *18*, A147–A160. [CrossRef] [PubMed]
72. Hwang, D.; Lee, H.; Jang, S.Y.; Jo, S.M.; Kim, D.; Seo, Y.; Kim, D.Y. Electrospray preparation of hierarchically-structured mesoporous TiO_2 spheres for use in highly efficient dye-sensitized solar cells. *ACS Appl. Mater. Interfaces* **2011**, *3*, 2719–2725. [CrossRef]
73. Hwang, D.; Kim, D.Y.; Jang, S.Y.; Kim, D. Superior photoelectrodes for solid-state dye-sensitized solar cells using amphiphilic TiO_2. *J. Mater. Chem. A* **2013**, *1*, 1228–1238. [CrossRef]
74. Alduraibi, M.; Hezam, M.; Al-Ruhaimi, B.; El-Toni, A.M.; Algarni, A.; Abdel-Rahman, M.; Qing, W.; Aldwayyan, A. Rapid room-temperature synthesis of mesoporous TiO_2 sub-microspheres and their enhanced light harvesting in dye-sensitized solar cells. *Nanomaterials* **2020**, *10*, 413. [CrossRef]